

manuscript submitted to *Geophysical Research Letters*

Convective self-compression of cratons and the stabilization of old lithosphere

¹Jyotirmoy Paul

²Clinton P. Conrad

^{3,4,5}Thorsten W. Becker

⁶Attrjee Ghosh

¹Bayerisches Geoinstitut, Universität Bayreuth

²Centre for Earth Evolution and Dynamics (CEED), Department of Geosciences, University of Oslo

³Institute for Geophysics, Jackson School of Geosciences, The University of Texas at Austin

⁴Department of Geological Sciences, Jackson School of Geosciences, The University of Texas at Austin

⁵Oden Institute for Computational Engineering & Sciences, The University of Texas at Austin

⁶Centre for Earth Sciences, Indian Institute of Science, Bangalore

Key Points:

- Mantle flow leads to inwardly convergent tractions around the edges of cratons, and compressive stress within.
- Convergent tractions result from the downward diversion of mantle flow.
- This convective self-compression could help stabilize older lithosphere against convective erosion.

Corresponding author: Jyotirmoy Paul, jyotirmoy.paul@uni-bayreuth.de

19 **Abstract**

20 Despite being exposed to convective stresses for much of the Earth's history, cratonic roots
 21 appear capable of resisting mantle shearing. This tectonic stability can be attributed to
 22 the neutral density and higher strength of cratons. However, the excess thickness of cra-
 23 tons and their higher viscosity amplify coupling to underlying mantle flow, which could
 24 be destabilizing. To investigate the stresses that a convecting mantle exerts on cratons
 25 that are both strong and thick, we developed instantaneous global spherical numerical
 26 models that incorporate present-day geoemtry cratons within active mantle flow. Our
 27 results show that mantle flow is diverted downward beneath thick and viscous cratonic
 28 roots, giving rise to a ring of elevated and inwardly-convergent tractions along a craton's
 29 periphery. These tractions induce regional compressive stress regimes within cratonic in-
 30 teriors. Such compression could serve to stabilize older continental lithosphere against
 31 mantle shearing, thus adding an additional factor that promotes cratonic longevity.

32 **Plain Language Summary**

33 Cratons are the oldest continental relicts on Earth. Due to plate tectonics and man-
 34 tle convection, many non-cratonic rocks get recycled. However, cratons have escaped tec-
 35 tonic recycling, and some have remained stable for more than ~ 3 billion years. Previ-
 36 ous studies have shown that cratons' high strength and neutral buoyancy provide them
 37 with tectonic stability. Here we show that the deep roots of cratons also help to stabi-
 38 lize them. This is because mantle flow is deflected downward beneath thick cratonic roots,
 39 and this deflection generates a ring of inwardly-directed forces around the edges of the
 40 craton. These inward forces compress the craton interior. Such self-induced compressive
 41 stresses may further help to stabilize Earth's oldest lithosphere.

42 **1 Introduction**

43 Cratons are relics of the oldest continental lithosphere, surviving since the Archean
 44 (Pearson & Wittig, 2014; Pearson et al., 1995; Pearson, 1999). Structurally, cratons have
 45 thick lithospheric roots, or cratonic keels (Gung et al., 2003; Polet & Anderson, 1995),
 46 that are likely cold because they are characterized by fast seismic velocities (Auer et al.,
 47 2014; Ritsema et al., 2011; Simmons et al., 2010). Low measured heat fluxes of cratonic
 48 lithosphere reaffirm the argument for colder cratons (Rudnick et al., 1998). The endurance
 49 of Archean cratons against Earth's tectonic and convective recycling is highly debated
 50 (cf. Yoshida & Yoshizawa, 2021), but proposed reasons for cratonic stability draw from
 51 geochemical and geophysical perspectives (Jordan, 1975, 1978; King, 2005; Lenardic &
 52 Moresi, 1999; Lenardic et al., 2003; Paul et al., 2019; Paul & Ghosh, 2020; Sleep, 2003;
 53 O'Neill et al., 2008; Wang et al., 2014; Yoshida, 2012). One of the oldest hypotheses pro-
 54 posed that cratons are constituted of chemically lighter elements that help them to float
 55 above the convective mantle without sinking into it (Jordan, 1975, 1978). However, sub-
 56 sequent numerical models showed that chemical buoyancy alone cannot protect cratons
 57 from the continuous convective shearing exerted by the mantle flow. Instead, root thick-
 58 ness and viscosity are the two prime factors that can resist deformation against man-
 59 tle shearing (Lenardic & Moresi, 1999; Lenardic et al., 2003; O'Neill et al., 2008; Paul
 60 et al., 2019; Paul & Ghosh, 2020; Sleep, 2003; Yoshida, 2012).

61 To understand the role of craton viscosity, previous studies quantified the nature
 62 of tractions exerted by mantle flow at the base of the lithosphere, and the strain-rates
 63 associated with deformation there (Conrad & Lithgow-Bertelloni, 2006; Cooper & Con-
 64 rad, 2009; Naliboff et al., 2009; Paul et al., 2019). Conrad & Lithgow-Bertelloni (2006)
 65 showed that tractions increase as the lithospheric thickness increases. Paul et al. (2019)
 66 found a similar amplification of tractions, but also showed that the strain-rates at the
 67 cratonic base diminish as lithospheric roots get thicker. This inverse relation between
 68 tractions and the strain-rates may slow the deformation of a cratonic root, and there-

fore might be an important factor for the long-term survival of cratons. Cooper & Conrad (2009) attributed elevated tractions at the base of cratons to greater coupling to mantle flow, which has been noted in models with thick cratonic roots (Zhong, 2001; Becker, 2006). However, more recent models, especially those employing free-slip surface boundary conditions that more closely resemble Earth's own conditions, show that tractions are primarily amplified along the periphery of cratons (fig. 3 from Paul et al., 2019). Although Paul et al. (2019) speculated that cratonic edges might more effectively absorb mantle stresses compared to cratonic interiors, a proper quantitative analysis of such a phenomenon is lacking.

Here, we explore the origin of higher tractions along craton boundaries and consider their implications for the stability of cratons. We build instantaneous global models of mantle convection and examine how mantle flow is modified due to the presence of thick and viscous cratons. We hypothesize that the diversion of mantle flow by the thick and highly viscous root of a craton can generate strong and inwardly-convergent tractions at the craton's periphery. We test our hypothesis using various models with different viscosity combinations for cratons and asthenosphere. We consider how large convergent tractions, which are generated by the cratons themselves, may support cratonic stability against mantle shearing, and therefore could be essential for cratonic longevity.

2 Mantle convection models

We use the finite element code CitcomS to develop instantaneous spherical models of mantle convection (Zhong et al., 2000). The code assumes the mantle to be a viscous and incompressible fluid. It solves the conservation of mass, momentum, and energy equations with the Boussinesq approximation and infinite Prandtl number. The smallest resolution of our models in the horizontal direction is $\sim 0.7^\circ \times 0.7^\circ$. The vertical resolution in the top 300 km is 24 km, and from 300 km to the CMB it is ~ 50 km. Mantle flow is driven by the density anomalies obtained from SMEAN2 seismic tomography (Jackson et al., 2017), which is a combination of S40RTS (Ritsema et al., 2011), GyPSuM-S (Simmons et al., 2010) and SAVANI (Auer et al., 2014). Following earlier, similar efforts (Becker, 2006; Paul & Ghosh, 2020), a velocity-density scaling value of 0.25 is used to convert velocity anomalies into density anomalies. Higher velocity regions under the continents were removed down to 300 km to impose neutrally buoyant cratons. We keep a free-slip boundary condition at the surface and at the core-mantle boundary. Reference viscosity, Rayleigh number (Zhong et al., 2000), thermal expansivity and thermal diffusivity values are kept at $\eta_{ref} = 10^{21}$ Pa.s, $Ra = 4 \times 10^8$ (considering Earth radius as the length scale), $\alpha = 3 \times 10^{-5}\text{K}^{-1}$, and $\kappa = 10^{-6}\text{m}^2/\text{s}$, respectively.

In our models, the mantle is divided into four layers based on their relative viscosity with respect to the upper mantle (300-600 km) reference viscosity (η_0). The top 100 km is assigned as the lithosphere, which is $30\times$ more viscous than the reference mantle viscosity. Asthenosphere(100-300 km) viscosity is varied between 0.01 (10^{19} Pa.s), 0.1 (10^{20} Pa.s) and 1 (10^{21} Pa.s) times the reference upper mantle viscosity. The lower mantle (660-2900 km) is made $50\times$ stronger than the reference mantle. On top of this radially-varying viscosity structure, we impose lateral viscosity variations. We approximate temperature-dependent viscosity using a linearised Arrhenius law $\eta = \eta_0 \times \exp(E(T_0 - T))$, where η_0 is the radial viscosity of any layer, T_0 is the non-dimensionalized reference temperature, and T is the non-dimensionalized actual temperature, where the maximum temperature corresponds to 1300°C . E is a dimensionless quantity that controls the strength of temperature dependence. We have tested several models to find suitable values for E (cf. Paul et al., 2019) and use a value of 5, which produces $10\times$ weak plate margins compared to the continental interiors. Weak plate margins originate due to slow velocity anomalies inherent within the SMEAN2 tomography model. Stronger continental interiors with weaker plate margins enhance plateness and produce plate velocities comparable to observations (fig. S1 of Paul et al., 2019). We also incorporate high viscosity cratons in our

models, where the locations of cratons are taken from the 3SMAC model (Nataf & Ricard, 1996). Cratons are made 10×, 100×, and 1000× more viscous than the surrounding lithosphere, and they have uniformly viscous keels up to a depth of 300 km. Our reference models omit cratons and only incorporate temperature-dependent viscosity to create lateral viscosity variations.

3 Tensions within cratons

We analyse the $r\phi$ and $r\theta$ components of stress tensor (σ_{ij} ; $i, j = r$: radial component, ϕ : longitudinal component, θ : co-latitudinal component) from model outputs and calculate traction vectors ($\vec{\tau}_0$) from the reference model (Fig. 1). In the reference model, the magnitudes of traction vectors are less than ~ 5 MPa, and their orientations are guided by density anomalies within the model (Fig. 1a). Incorporating 100× viscous cratons in the same model significantly affects traction vectors ($\vec{\tau}$) along the edges of cratons (Fig. 1b). A few enlarged maps near the cratonic regions show this effect more prominently (Figs. 1c-i). Most cratons show rings of high traction magnitude along their periphery, where traction directions become inwardly convergent. Elevated inwardly convergent tractions appear prominently along the western margin of the North and South American cratons (Figs. 1c,d), the northern and southern margins of the Scandinavian craton (Fig. 1f), the eastern, western and southern margins of the Siberian and Australian cratons (Figs. 1e,g), and the eastern margins of African cratons (Fig. 1h). The Indian craton, being very small in size, experiences convergent tractions all around its periphery (Fig. 1i). The southernmost part of the African craton shows an outwardly directed traction, which is the only exception (Fig. 1h). We have tested a model with high lithospheric viscosity (150×) and similarly found large traction ratios along cratons' periphery (Fig. S1).

To quantify the increase in traction magnitudes caused by the presence of cratons, we normalize the traction magnitudes from models with cratons using those from the reference model ($|\vec{\tau}|/|\vec{\tau}_0|$). In the presence of cratons that are 100× more viscous than the rest of the lithosphere, the maximum traction ratio increases by up to 80-100 times at ~ 120 km depth along the edges of cratons (Fig. 1c-i). The magnitude of the traction ratio along the craton edges can be influenced by the viscosity structure imposed in our models (Figs. 2). To investigate the dependence of the traction ratio on viscosity structure and depth, we calculate the average traction ratio at various depths along the edges of cratons (Fig. 2a). The edges of cratons are identified by regions with traction ratio ($|\vec{\tau}|/|\vec{\tau}_0|$) more than 5 at 120 km depth (Figs. 1c-i). The general trend shows that the average traction ratio varies between 10 and 15 within the top 100 km of craton edges (Fig. 2a), which are proximal to viscous non-cratonic lithosphere. The average traction ratios increase with depth, reaching peak values in the mid-cratonic depth range of ~ 160 km. The highest traction ratio occurs near the depth of peak horizontal velocity, which occurs in the mid-asthenosphere. With increasing depth, the traction ratio gradually falls before reaching another smaller peak near the base of cratons at ~ 270 km depth (Fig. 2a). The magnitude of the traction ratio depends on the combination of the craton and asthenosphere viscosity. Higher viscosity contrast between a craton and its surroundings can enhance traction ratio. Indeed, highly viscous (1000×) cratons exhibit the largest traction ratios, which exhibit peak values of 35-45 for mid-asthenospheric depths. Models with smaller viscosity contrasts (e.g., stronger asthenosphere with relative viscosity 1×) exhibit relatively smaller traction ratios near the craton edges.

We use centroid moment tensor (CMT) type symbols (Fig. 1) to quantify the state of stress within cratons due to inwardly convergent tractions. CMT symbols are colored by the ratio of mean horizontal stress ($\sigma_h = \frac{1}{2}(\sigma_{\phi\phi} + \sigma_{\theta\theta})$) and the second invariant of the deviatoric stress ($\sigma_{II} = \sqrt{\sigma_{ij}\sigma_{ij}}$). A negative ratio ($\sigma_h/\sigma_{II} < 0$) indicates a compressive stress regime and vice-versa. The deformation states shown imply that the model without cratons (Fig. 1a) has compression only along the convergent plate boundaries,

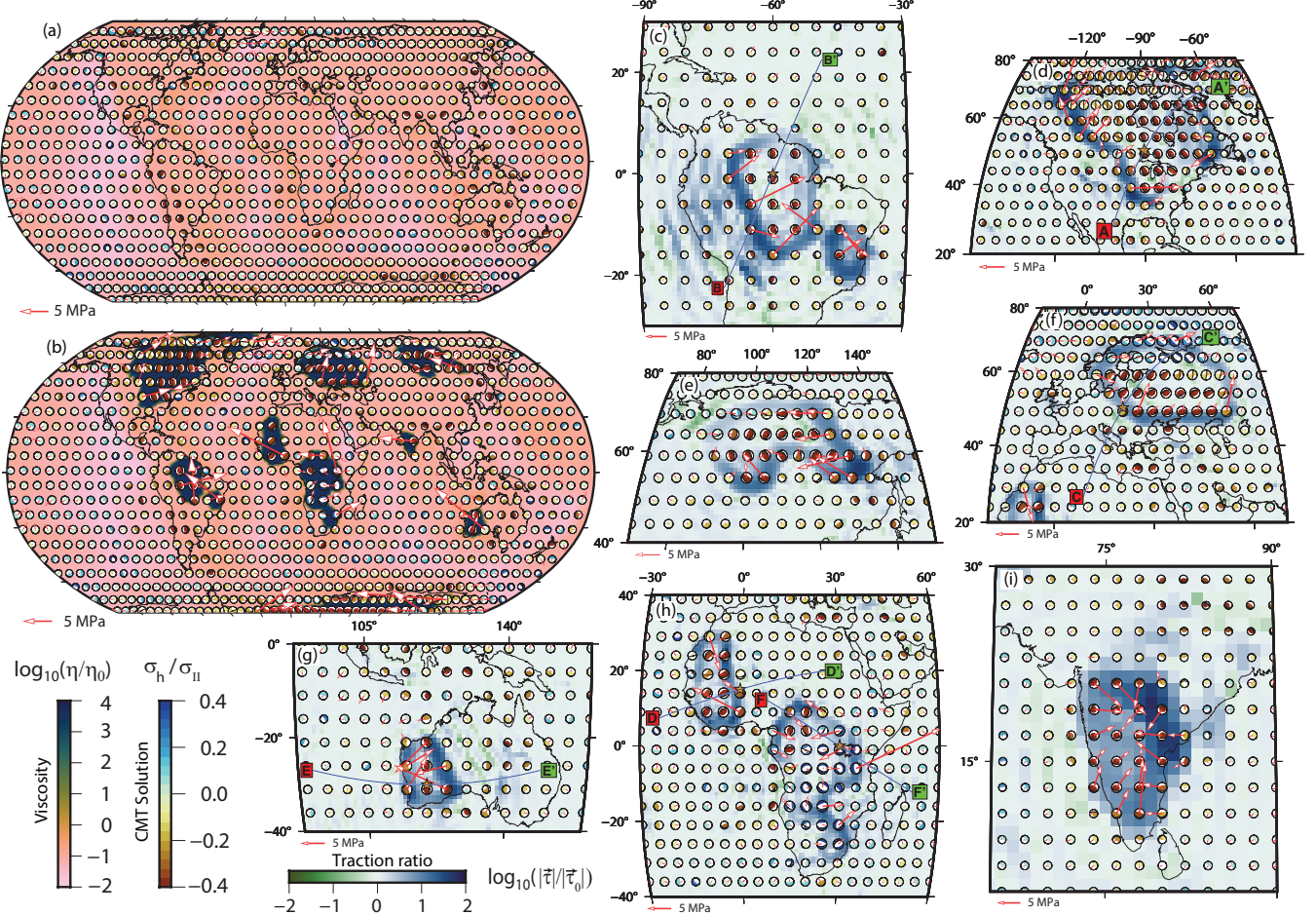


Figure 1. Global traction patterns and stress regimes in the absence and presence of cratons at 120 km depth. (a) Traction in the reference model (relative viscosity of asthenosphere is 0.1) without cratons, (b) Traction in a model with 0.1 relative viscosity of asthenosphere and cratons that are 100× more viscous than the surrounding lithosphere. Background colors in the global plots (a-b) indicate viscosity, and arrows represent the magnitude and direction of absolute traction. CMT symbols are colored as the ratio of mean horizontal stress to the second invariant of deviatoric stress (σ_h/σ_{II}), where negative values represent compressive stress regimes. (c)-(i) Zoomed-in plots near the cratonic regions of South America (c), North America (d), Siberia (e), Scandinavia (f), Australia (g), Africa (h), and India (i). The background colors in (c-i) represent the logarithm of the traction ratio ($\log_{10}(|\vec{\tau}|/|\vec{\tau}_0|)$). Velocity cross-sections along the six transects (AA' - FF') are shown in Fig. 4.

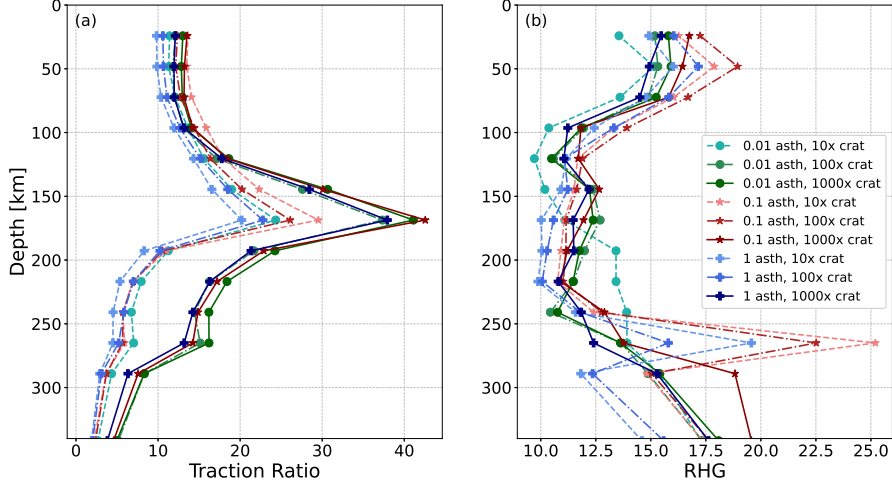


Figure 2. (a) Depth variation of the average traction ratio along the craton periphery (defined as regions where $|\vec{\tau}|/|\vec{\tau}_0| > 5$ at 120 km depth for different models. (b) Depth variation of the ratio of the horizontal velocity gradient (RHG) within regions having RHG value > 5 . A description of the different models is given in the index box. The first number in the box indicates the relative viscosity of the asthenosphere, and the second number indicates the viscosity of cratons with respect to the lithosphere.

i.e., along the margins of the Pacific and the Indo-Eurasia collision zones. The same model with $100\times$ viscous cratons (Figs. 1b-i) acquires a compressive stress regime within all cratons, except in South Africa (Fig. 1h).

4 Origin of compression along craton edges

Our models demonstrate an amplification of tractions ($\vec{\tau}$) along craton edges that induce a highly compressive state within viscous cratons. To understand the origin of this regional compressive stress regime, we calculate the traction vector ($\vec{\tau}$) from the $\sigma_{r\phi}$ and $\sigma_{r\theta}$ components of the deviatoric stress tensor that relate to horizontal shear,

$$\sigma_{r\phi} = 2\eta \left(\frac{\partial v_\phi}{\partial r} + \frac{\partial v_r}{\partial \phi} \right) \quad (1)$$

$$\sigma_{r\theta} = 2\eta \left(\frac{\partial v_\theta}{\partial r} + \frac{\partial v_r}{\partial \theta} \right) \quad (2)$$

where v_ϕ , v_θ , and v_r are the horizontal and vertical components of the velocity vector and η is the viscosity. If these shear components dominate the stress tensor, then the magnitude of horizontal traction is given by

$$|\vec{\tau}| = 2\eta \sqrt{\left(\frac{\partial v_\phi}{\partial r} + \frac{\partial v_r}{\partial \phi} \right)^2 + \left(\frac{\partial v_\theta}{\partial r} + \frac{\partial v_r}{\partial \theta} \right)^2} \quad (3)$$

The presence of a thick and highly viscous craton obstructs horizontal asthenospheric flow, and deflects it downward near the craton edges. Such velocity diversion can make the $\frac{\partial v_\phi}{\partial r}$ and $\frac{\partial v_\theta}{\partial r}$ components small near the craton edges, implying that the first terms in equations 1 and 2 can be neglected. With stronger downward diversion, the vertical

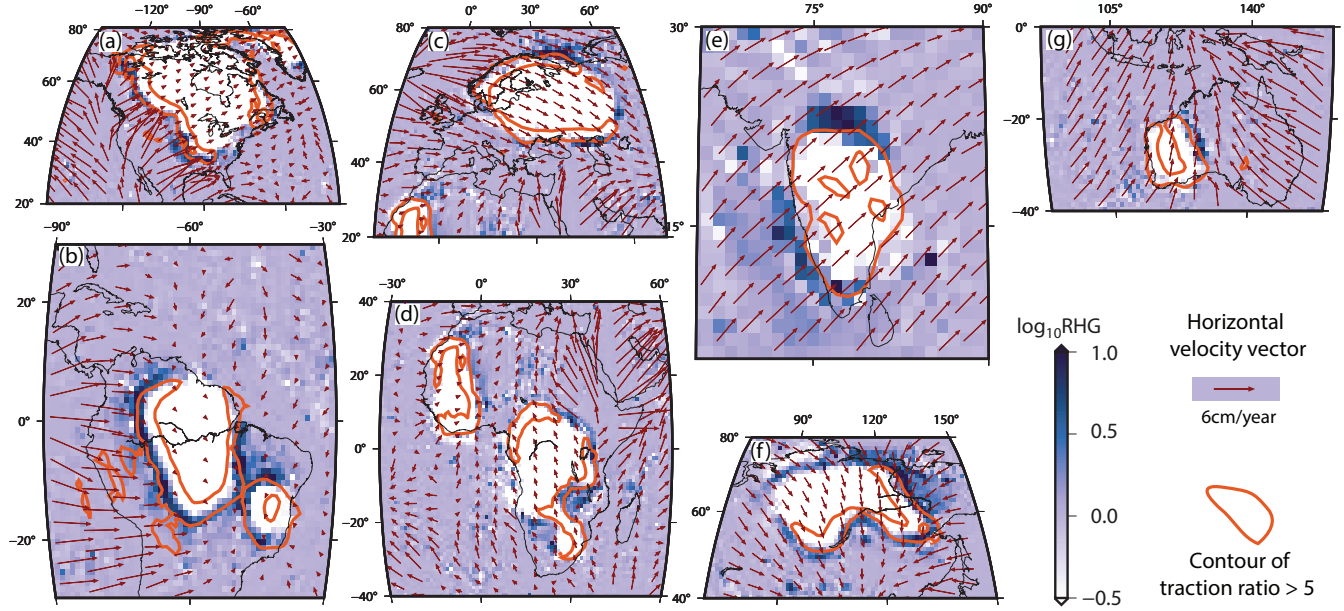


Figure 3. Zoomed-in maps of the ratio of horizontal gradients of vertical velocity (RHG) at 120 km depth near different cratonic regions from model with 0.1 relative viscosity of asthenosphere and 100× more viscous cratons than the surrounding lithosphere. Horizontal velocity vectors at 120 km depth are plotted on top of it. Orange lines encircle areas where $|\vec{v}|/|\vec{v}_0| > 5$ at 120 km depth.

velocity (v_r) increases approaching a craton edge. Thus, the horizontal gradient of the vertical velocity component, i.e., the second term in equations 1 and 2, becomes the controlling factor for the origin of high tractions along craton boundaries. A small change in velocity gradients near cratons can thus induce higher tractions around them as tractions originate from velocity gradients multiplied by the high viscosity of cratons (equation 3).

Large horizontal gradients of vertical velocities, induced by viscosity heterogeneity associated with cratons, thus amplify tractions. We calculate such gradients as:

$$\nabla_h^V = \sqrt{\left(\frac{\partial v_r}{\partial \phi}\right)^2 + \left(\frac{\partial v_r}{\partial \theta}\right)^2} \quad (4)$$

To highlight the impact of thick cratons on the gradient, we compute the ratio of the horizontal velocity gradient (RHG) as:

$$RHG = \frac{(\nabla_h^V)_{\text{craton}}}{(\nabla_h^V)_{\text{no_craton}}} \quad (5)$$

where $(\nabla_h^V)_{\text{craton}}$ and $(\nabla_h^V)_{\text{no_craton}}$ are the horizontal gradient of vertical velocities from models with and without cratons, respectively. RHG can quantify the concentration of downward flow due to the presence of viscous cratons, where $RHG \gg 1$ indicates strong vertical velocity deflection.

Similar to the rings of high traction zones, we find rings of elevated RHG along the craton periphery (Fig. 3). Elevated RHG values can be interpreted as horizontal velocities converting into vertical velocities near the craton boundary due to cratons' excess thickness and viscosity. Horizontal gradients of vertical velocity should amplify tractions,

and indeed contours of traction ratio > 5 typically lie next to regions of high RHG values (Fig. 3). The reduction of horizontal velocity at craton edges is clearly visible underneath North and South America (Figs. 3a,b). The strong velocity decrease arises because slabs underneath these two cratons force a rapid asthenospheric flow that is impeded by stiff cratons. The velocity gradient variations expressed by RHG are also controlled by the angle between the craton edge and the direction of horizontal flow. In our density-driven flow models, the mantle flows from west to east under the North American plate, remaining almost perpendicular to the western face of the craton (Fig. 3a). Hence, the maximum velocity diversion, or highest RHG value, occurs along the western margin of the North American craton. On the contrary, the southeastern margin of the craton, being almost parallel to flow, shows no significant change in RHG values. This pattern resembles the change of traction vectors along the western and eastern margins of the North American craton (Fig. 1d), where elevated tractions are observed, but not on the southern and northern margins. Other cratonic edges with large RHG values include the western margins of the South American (Fig. 3b) and Indian (Fig. 3e) cratons, the northern and Southern margins of the Scandinavian craton (Fig. 3c), the eastern margins of the African cratons (Fig. 3d,e), and the eastern and northern margins of the Siberian (Fig. 3f) and Australian (Fig. 3g) cratons.

To investigate how downwelling on the craton edges varies with depth and viscosity structure, we calculate variations of average RHG within the region where RGH value > 5 . In the top 100 km, the average RHG varies within 15-17. In the mid-cratonic depth range (100-250 km), the average RHG value decreases to slightly less than 12.5. Deeper than 250 km depth, RHG increases again, reaching a peak near the base of cratons. These two peaks near the top and bottom of craton may appear due to the most significant change of velocity gradients occurring above and below the asthenosphere, giving rise to a 'z' type velocity profile, considering left to right horizontal flow (e.g., Fig. 4d).

We compare the velocity cross-sections from our models with and without cratons (Figs. 4) to investigate the actual nature of flow diversion along craton edges. Such flow has been attributed to edge-driven convection previously (e.g. King & Ritsema, 2000), but our results suggest that flow diversion is a natural consequence of global mantle convection operating in the presence of lithospheric viscosity heterogeneity. Cross-sections underneath the South American and the North American cratons show the most notable changes in velocity along their western margins (Figs. 4a-d). In both cases, the mantle flows from west to east in the absence of a craton due to density heterogeneity present in our models (Figs. 4a,c). Convergent flow west of the South American craton occurs due to the subducting Nazca slab. In the presence of a thick and viscous craton, the convergent flow velocity is diverted along the craton margin and gets concentrated below it (Fig. 4b). Similar velocity diversion is also visible around the western margin of the North American craton, where the flow gets diverted downwards and concentrated below the craton (Fig. 4d). Flow diversion by the Scandinavian craton occurs along a north-south orientation (Figs. 4e,f). However, the diversion is relatively weaker most likely due to the absence of nearby mantle slabs to drive the flow in the model. Weaker velocity diversion is also reflected in less elevated traction magnitudes compared to the American cratons. The size of the Western African craton is significantly smaller than the rest, but the change of velocity field is considerably pronounced (Figs. 4g,h). A downward flow along the Eastern margin of the craton denotes the change in RHG (Fig. 4h). The Australian craton also shows velocity diversion (Figs. 4i,j) along an east west profile, leading to amplified tractions. The South African craton is different from the other cratons because of upwelling mantle flow below it (Fig. 4f). In this scenario, the horizontal velocities get diminished due to the craton, and vertical upward velocities on the eastern side become stronger along the craton boundary. Therefore, the traction magnitudes increase along the South African craton's southeastern margin, as it does for the other cratons, but the tractions are outwardly directed and the stress regime becomes extensional (Fig. 1h).

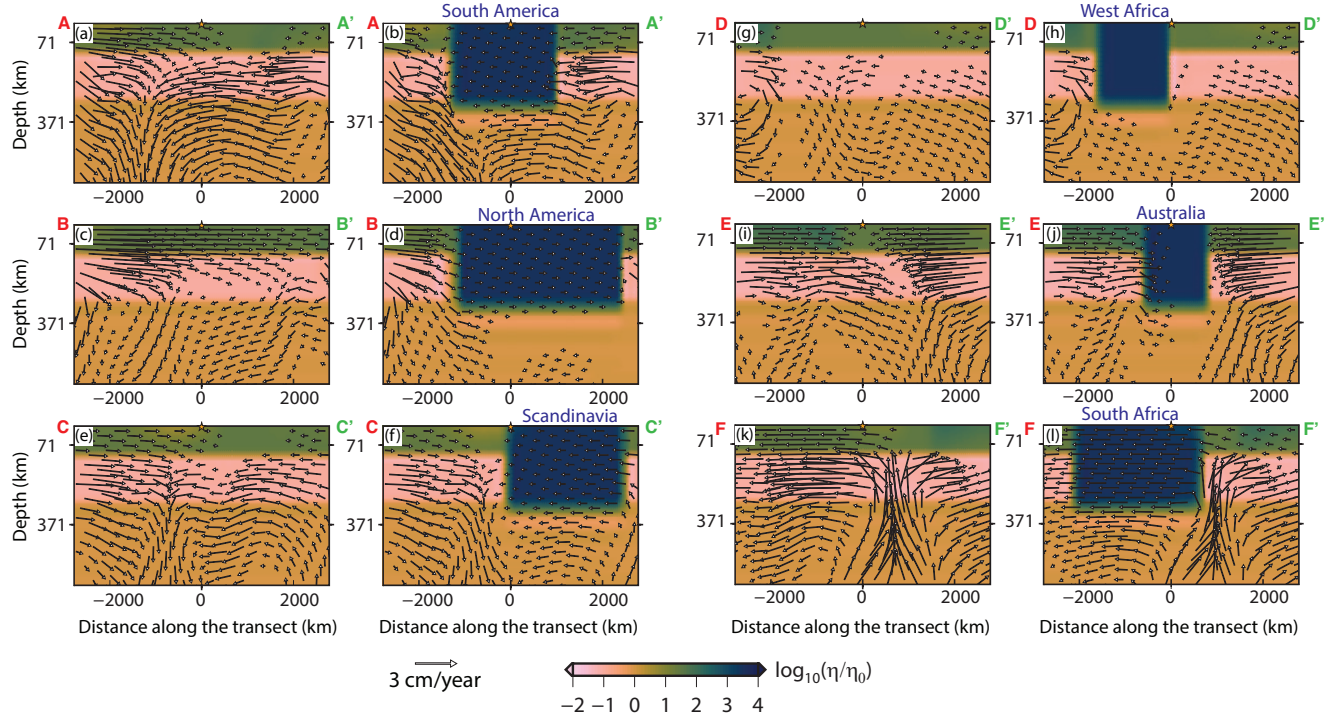


Figure 4. Comparison of velocity cross-sections up to 600 km with and without cratons along the transects shown in Figs. 1c-i. Each figure is paired where the left figure shows the velocity profile without a stiff craton, and the right figure shows the same with craton. The name of the continental mass that contains the craton is given for all corresponding right-side figures. Background colors represent the logarithm of relative viscosity, and the arrows represent velocity vectors along the transect.

5 Conclusions

The diversion of mantle flow by thick and viscous cratonic lithosphere induces self-compression within the cratons themselves. Traction magnitudes increase along the craton periphery, and their directions become convergent toward craton interiors. Traction magnitudes depend on the viscosity structure of the craton, asthenosphere, and lithosphere. In the presence of a 100× viscous craton, traction magnitude increases to 15–20 MPa (Figs. 1b-i), more than an order of magnitude larger than cases without cratons (Fig. 1a). The inward-directed orientation of tractions along the craton boundary appears to be a universal phenomenon (Figs. 1b, S1), except for the southern most part of the African craton (Fig. 1h). We infer that such convergent tractions originate from the diversion of (typically downward) mantle flow due to thick and viscous cratonic roots. We test our hypothesis by calculating the ratio of the horizontal gradient of vertical velocity (RHG, equation 5). Our calculations demonstrate that large velocity gradients along craton margins amplify tractions along the craton periphery. For most cratons the downward diversion of mantle flow produces inward-directed tractions that induce a compressive stress regime within all cratons. The South African craton presents the only exception, where upwelling flow generates extension.

Previous studies have attributed the long-term stability of cratons to the combined effect of increased thickness, elevated viscosity, and chemical buoyancy (Lenardic et al., 2003; Paul et al., 2019). We suggest that self-induced compressive tractions along craton boundaries could be another critical factor that have made cratons stable across bil-

manuscript submitted to *Geophysical Research Letters*

lions of years. Geologically, cratons are not individual single units; instead, they are composed of multiple protocratons that together form a larger continental mass (Bleeker, 2003). For example, the North American craton is composed of the Superior, Slave, Wyoming, Hearne, Rae, and several other small blocks (Canil et al., 2008); the Indian craton is assembled with five smaller units, Dharwar, Bastar, Singhbhum, Bundelkhand, and Aravalli (Pandey, 2020). Since their formation and amalgamation, larger continental units have remained together for more than a couple of billion years. There are some instances of delamination or partial destruction of cratons (Liu et al., 2021; Menzies et al., 1993), but none of them were completely split apart. Self-compression could help to keep smaller continental blocks together within larger cratonic units. It also may be a key reason that older continental units did not split away during supercontinental break-up events. In the future, time-dependent numerical models should be developed to study the effect of self-compression in the craton stabilization process.

295 **Acknowledgments**

296 The finite element code CitcomS code is maintained by Computational Infrastructure
 297 for Geodynamics (<https://geodynamics.org/>). All models were developed in Cray XC40
 298 system at the Supercomputer Education and Research Centre (SERC), IISc. The expenses
 299 for the high-priority computational facility was supported by grant IE/REDA-20-1994
 300 to AG from the Indian Institute of Science–Institution of Eminence (IISc-IOE). JP was
 301 partially funded by grant SP/DSTO-20-0014 from the Department of Science and Tech-
 302 nology (DST), Govt. of India. This work was partially supported by the Norwegian Re-
 303 search Council projects 223272 (Centre of Excellence) and 288449 (MAGPIE Project).
 304 TWB was partially support by NSF EAR 1925939 and 1853856. JP acknowledges De-
 305 banjan Pal for helping with data management and running a few accessory models for
 306 this project. Figures were prepared using GMT 6.0.0 and python. The research publi-
 307 cation is supported by the Open Access Publication Fund of the University of Bayreuth.

308 **Open Research**

309 The latest version of CitcomS code is freely available for download on GitHub (<https://github.com/geodynamics/citcoms>). Example input files and the model output can be
 310 downloaded from JP's personal GitHub repository: <https://jyotirmoyp.github.io/research/craton/> or <https://doi.org/10.5281/zenodo.7264900>. Detailed mathe-
 311 matical calculations and formulations are given in text which can be used to reproduce
 312 the results.
 313

315 **References**

- 316 Auer, L., Boschi, L., Becker, T., Nissen-Meyer, T., & Giardini, D. (2014). Savani:
 317 A variable resolution whole-mantle model of anisotropic shear velocity varia-
 318 tions based on multiple data sets. *Journal of Geophysical Research: Solid Earth*,
 319 119(4), 3006–3034.
- 320 Becker, T. W. (2006). On the effect of temperature and strain-rate dependent vis-
 321 cosity on global mantle flow, net rotation, and plate-driving forces. *Geophysical
 322 Journal International*, 167(2), 943–957.
- 323 Bleeker, W. (2003). The late Archean record: a puzzle in ca. 35 pieces. *Lithos*, 71(2-
 324 4), 99–134.
- 325 Canil, D., et al. (2008). Canada's craton: a bottoms-up view. *GSA TODAY*, 18(6),
 326 4–10.
- 327 Conrad, C. P., & Lithgow-Bertelloni, C. (2006). Influence of continental roots and
 328 asthenosphere on plate-mantle coupling. *Geophysical Research Letters*, 33, L05
 329 312, doi:10.1029/2005GL025621.
- 330 Cooper, C., & Conrad, C. P. (2009). Does the mantle control the maximum thick-
 331 ness of cratons? *Lithosphere*, 1(2), 67–72.
- 332 Gung, Y., Panning, M., & Romanowicz, B. (2003). Global anisotropy and the thick-
 333 ness of continents. *Nature*, 422(6933), 707–711.
- 334 Jackson, M. G., Konter, J. G., & Becker, T. W. (2017). Primordial helium entrained
 335 by the hottest mantle plumes. *Nature*, 542, 340–343.
- 336 Jordan, T. (1975). The continental tectosphere. *Reviews of Geophysics*, 13(3), 1–
 337 12.
- 338 Jordan, T. (1978). Composition and development of the continental tectosphere. *Na-
 339 ture*, 274(5671), 544–548.
- 340 King, S. (2005). Archean cratons and mantle dynamics. *Earth and Planetary Sci-
 341 ence Letters*, 234(1), 1–14.
- 342 King, S., & Ritsema, J. (2000). African hot spot volcanism: small-scale convection
 343 in the upper mantle beneath cratons. *Science*, 290(5494), 1137–1140.
- 344 Lenardic, A., & Moresi, L. N. (1999). Some thoughts on the stability of cratonic

- 345 lithosphere: effects of buoyancy and viscosity. *Journal of Geophysical Research: Solid Earth*, 104(B6), 12747–12758.
- 346 Lenardic, A., Moresi, L. N., & Mühlhaus, H. (2003). Longevity and stability of
347 cratonic lithosphere: insights from numerical simulations of coupled mantle con-
348 vention and continental tectonics. *Journal of Geophysical Research: Solid Earth*,
349 108(B6), <https://doi.org/10.1029/2002JB001859>.
- 350 Liu, J., Pearson, D. G., Wang, L. H., Mather, K. A., Kjarsgaard, B. A., Schaeffer,
351 A. J., ... Armstrong, J. P. (2021). Plume-driven re-cratonization of deep continen-
352 tal lithospheric mantle. *Nature*, 592(7856), 732–736.
- 353 Menzies, M. A., Fan, W., & Zhang, M. (1993). Palaeozoic and Cenozoic lithoprobes
354 and the loss of c. 120 km of Archaean lithosphere, Sino-korean craton, China. *Geo-
355 logical Society, London, Special Publications*, 76(1), 71–81.
- 356 Maliboff, J. B., Conrad, C. P., & Lithgow-Bertelloni, C. (2009). Modification of the
357 lithospheric stress field by lateral variations in plate-mantle coupling. *Geophysical
358 Research Letters*, 36(22), L22307, doi:10.1029/2009GL040484.
- 359 Nataf, H.-C., & Ricard, Y. (1996). 3SMAC: an a priori tomographic model of the
360 upper mantle based on geophysical modeling. *Physics of the Earth and Planetary
361 Interiors*, 95(1–2), 101–122.
- 362 O'Neill, C., Lenardic, A., Griffin, W., & O'Reilly, S. (2008). Dynamics of cratons in
363 an evolving mantle. *Lithos*, 102(1), 12–24.
- 364 Pandey, O. P. (2020). *Geodynamic evolution of the Indian shield: Geophysical aspects*. Springer, <https://doi.org/10.1007/978-3-030-40597-7>.
- 365 Paul, J., & Ghosh, A. (2020). Evolution of cratons through the ages: A
366 time-dependent study. *Earth and Planetary Science Letters*, 531, 115962,
367 <https://doi.org/10.1016/j.epsl.2019.115962>.
- 368 Paul, J., Ghosh, A., & Conrad, C. (2019). Traction and strain rate at the base
369 of the lithosphere: An insight into cratonic stability. *Geophysical Journal Interna-
370 tional*, 217(2), 1024–1033.
- 371 Pearson, D. (1999). The age of continental roots. *Lithos*, 48(1), 171–194.
- 372 Pearson, D., Carlson, R., Shirey, S., Boyd, F., & Nixon, P. (1995). Stabilisation of
373 Archaean lithospheric mantle: A Re-Os isotope study of peridotite xenoliths from
374 the Kaapvaal craton. *Earth and Planetary Science Letters*, 134(3), 341–357.
- 375 Pearson, D., & Wittig, N. (2014). The formation and evolution of cratonic mantle
376 lithosphere—evidence from mantle xenoliths. In K. Turekian & H. Holland (Eds.),
377 *Treatise on geochemistry* (p. 255–292). New York: Elsevier.
- 378 Polet, J., & Anderson, D. (1995). Depth extent of cratons as inferred from tomo-
379 graphic studies. *Geology*, 23(3), 205–208.
- 380 Ritsema, J., Deuss, A. A., Van Heijst, H., & Woodhouse, J. (2011). S40RTS: a
381 degree-40 shear-velocity model for the mantle from new Rayleigh wave disper-
382 sion, teleseismic traveltimes and normal-mode splitting function measurements.
383 *Geophysical Journal International*, 184(3), 1223–1236.
- 384 Rudnick, R., McDonough, W., & O'Connell, R. (1998). Thermal structure, thickness
385 and composition of continental lithosphere. *Chemical Geology*, 145(3), 395–411.
- 386 Simmons, N. A., Forte, A. M., Boschi, L., & Grand, S. P. (2010). GyPSuM: A
387 joint tomographic model of mantle density and seismic wave speeds. *Journal of
388 Geophysical Research: Solid Earth*, 115, <https://doi.org/10.1029/2010JB007631>.
- 389 Sleep, N. H. (2003). Survival of Archean cratonal lithosphere. *Journal of Geophysical
390 Research: Solid Earth*, 108(B6), 2302, doi:10.1029/2001JB000169.
- 391 Wang, H., van Hunen, J., Pearson, D. G., & Allen, M. B. (2014). Craton stability
392 and longevity: The roles of composition-dependent rheology and buoyancy. *Earth
393 and Planetary Science Letters*, 391, 224–233.
- 394 Yoshida, M. (2012). Dynamic role of the rheological contrast between cratonic and
395 oceanic lithospheres in the longevity of cratonic lithosphere: A three-dimensional
396 numerical study. *Tectonophysics*, 532, 156–166.

manuscript submitted to *Geophysical Research Letters*

- 399 Yoshida, M., & Yoshizawa, K. (2021). Continental drift with deep cratonic roots.
400 *Annual Review of Earth and Planetary Sciences*, 49, 117–139.
- 401 Zhong, S. (2001). Role of ocean-continent contrast and continental keels on plate
402 motion, net rotation of lithosphere, and the geoid. *Journal of Geophysical Re-*
403 *search: Solid Earth*, 106(B1), 703–712.
- 404 Zhong, S., Zuber, M., Moresi, L. N., & Gurnis, M. (2000). Role of temperature-
405 dependent viscosity and surface plates in spherical shell models of mantle convec-
406 tion. *Journal of Geophysical Research: Solid Earth*, 105(B5), 11063–11082.